

# OPTIMIZATION OF THE DESIGN OF OMNIS, THE OBSERVATORY OF MULTIFLAVOR NEUTRINOS FROM SUPERNOVAE

J. J. Zach<sup>a</sup> A. St. J. Murphy<sup>a</sup> D. Marriott<sup>a</sup> R. N. Boyd<sup>a,b</sup>

<sup>a</sup>*Department of Physics, Smith Laboratory, 174 W. 18th Ave., Columbus, OH,  
43210*

<sup>b</sup>*Department of Astronomy, 140 W. 18th Avenue, Columbus, OH, 43210*

---

## Abstract

A Monte Carlo code has been developed to simulate the operation of the planned detectors in OMNIS, a supernova neutrino observatory. OMNIS will detect neutrinos originating from a core collapse supernova by the detection of spalled neutrons from Pb- or Fe-nuclei. This might be accomplished using Gd-loaded liquid scintillator. Results for the optimum configuration for such modules with respect to both neutron detection efficiency and cost efficiency are presented. Careful consideration has been given to the expected levels of radioactive backgrounds and their effects. The results show that the amount of data to be processed by a software trigger can be reduced to the  $< 10$  kHz region and a neutron, once produced in the detector, can be detected and identified with an efficiency of  $> 30\%$ .

*Key words:* Supernovae; Monte Carlo; neutrino detector; neutron detector; liquid scintillator

PACS: 14.60.Pq, 29.40.Mc, 29.85.+c, 97.60.Bw

---

## 1 Introduction

The electron-antineutrinos observed by the Kamiokande (1) and IMB (2) laboratories from supernova 1987-A confirmed that neutrinos play an important role in core collapse supernovae. The vast majority of the gravitational binding energy of the protoneutron star is radiated away by neutrinos. The observed  $\bar{\nu}_e$  were detected over a few seconds, much longer than the weak interaction time-scales which are thought to be required to produce them.

This confirmed the main features of the standard model of core-collapse supernovae (3) and suggests that the behavior of the neutrino opacity in matter beyond nuclear densities is understood (4). As has been shown in numerous supernova simulations (see, e.g. (5)), the shock that will produce the supernova stalls, thus disfavoring a prompt mechanism (6). Although there are many uncertainties in the calculations, indications that the shock has to be revived by neutrinos are strong (7).

An increasing body of data from the atmospheric neutrino experiments at Super-Kamiokande (8), IMB (9), Soudan2 (10) and Kamiokande (11), exhibit the disappearance of  $\mu$ -neutrinos (12). Solar neutrino experiments such as Homestake (13), Kamiokande (14), GALLEX (15), SAGE (16) and Super-Kamiokande (17) also suggest a flux of  $\nu_e$ 's inconsistent with the Bahcall-Pinsonneault standard solar model. The most favored solution to these discrepancies is an extension of the standard model of particle physics to one in which the neutrinos have mass and are allowed to oscillate between flavors via the vacuum and/or the Mikheyev-Smirnov-Wolfenstein (MSW-) oscillation mechanisms (18). Direct measurements of the neutrino masses (19) yield upper limits of  $m_{\nu_e} \leq 3 \text{ eV}$  (90%CL),  $m_{\nu_\mu} \leq 170 \text{ keV}$  (90%CL) and  $m_{\nu_\tau} \leq 18.2 \text{ MeV}$  (95%CL). However, the tremendous neutrino luminosities of supernovae provide a unique scenario for extremely long baseline measurements, allowing a vastly increased region of neutrino mixing parameter space to be probed, and placing more stringent limits than can otherwise be achieved on neutrino masses and mixing angles.

The astrophysical r-process may also depend critically on the properties of neutrinos. The leading candidate for its site is the low-density, high-entropy bubble of a core-collapse supernova, created in the trail of the outgoing shock-wave by material lifted off the surface of the protoneutron star and heated by neutrinos (20; 21). The details of the interaction between the neutrinos and matter in the bubble are highly nonlinear, and may require several types of MSW-type oscillations (22; 23).

## 2 Motivation and Properties of OMNIS

### 2.1 *The Role of OMNIS in the Supernova Neutrino Observatory Community*

An observation of the fluxes of different neutrino flavors is vital for the understanding of core-collapse supernovae and helpful for the investigation of new physics beyond the standard model. In this context, the need for a large neutral-current neutrino detector has become increasingly obvious in recent years (24). Accordingly, OMNIS is being designed to provide a much

larger sample of  $\mu$ - and  $\tau$ -neutrino events than would be provided by other detectors, allowing a significantly more detailed measurement of the neutrino spectra for different flavors, resolved in time, and the stellar conditions that produced them. Given the planned quantities of iron and lead, and with the detection strategy suggested here, a typical supernova at the center of the Galaxy would lead to about 2000 observed events in OMNIS (25) (assuming no oscillations), predominantly from *neutral-current* reactions. These events will provide a window for looking well beyond the peak of the supernova neutrino burst to study the evolution at times up to  $\approx 10$  *seconds* after the start of the pulse, a potentially important diagnostic of the cooling mechanism. A few thousand events are also adequate for accurate neutrino mass measurements.

Most present neutrino detectors, such as Super-Kamiokande, LVD, MACRO and AMANDA, are primarily sensitive to charged-current channels, involving mainly the reaction of  $\bar{\nu}_e$  with protons in water or mineral oil. Super-Kamiokande will also see some  $e$ -neutrinos and some  $\mu$ - and  $\tau$ -neutrinos through the detection of  $\gamma$ -rays produced in the neutral-current channels  $^{16}\text{O}(\nu, \nu'p/n\gamma)$ , as suggested by Langanke and Vogel (26). The total number of detected neutral-current events due to  $\mu$ - and  $\tau$ -neutrinos for a core-collapse supernova at a distance of 8 *kpc* has been estimated to be around 300 or 560, depending upon the temperature and chemical potential in the neutrino Fermi-Dirac distribution assumed. Recent changes to the data acquisition that result in a lower detection threshold might improve this to around 1000 events (27). However, this yield comes from a single reaction threshold and so the unknown neutrino energy distribution cannot be inferred. SNO, which is designed around a tank of heavy water, would be expected to produce around 750 break-up events of deuterium following neutrino neutral-current scattering for a supernova at the same distance (28). It is on the other hand scheduled for a lifetime at the low edge of the mean time between Galactic supernovae (10-30 years, (30)), even though SNO's scheduled time has been extended from two to ten years.

It has been shown (28) that, based on time-of-flight information, Super-Kamiokande and SNO will have resolutions of  $m_{\nu_{\mu/\tau}} \approx 50$  *eV* and  $m_{\nu_{\mu/\tau}} \approx 30$  *eV*, respectively, although again the improved statistics due to a lower detection threshold will improve considerably the value for Super-Kamiokande. Due to both the greater number of neutral-current events detected, and to its superior timing capability, OMNIS is expected to have a still better mass resolution of around 20 *eV*.

A particularly interesting scenario is that in which a Galactic core-collapse supernova proceeds to a black hole. This should produce an abrupt termination of neutrino flux as well as several remarkable measurements. Firstly, the signal preceding the cut-off, and when the signal occurs may depend on the protoneutron star evolution, and hence the equation of state (29). Secondly, as the black hole expands outward from the center of the star it will envelope

successive neutrinospheres (29). One might therefore expect the  $\nu_{\mu/\tau}$ -flux to be terminated earlier than the  $\bar{\nu}_e$ -flux which would in turn occur before the termination of the  $\nu_e$ -flux. The difference in time between these terminations has been estimated to be of order 1 *ms* (29). If the supernova is close enough, OMNIS would be able to observe these differences, and thus could infer the structure of the neutrinospheres. Lastly, the termination of the luminosity provides a well defined feature that would provide an opportunity for time-of-flight mass measurements of the neutrino mass with unparalleled accuracy, down to limits of 2 *eV* for  $\bar{\nu}_e$  in Super-Kamiokande and as low as 4 *eV* for  $\mu$ - and  $\tau$ -neutrinos from OMNIS (30).

## 2.2 *Expected Neutrino Signal from a Core-Collapse Supernova*

In order to make estimates of the response of the OMNIS detectors to a supernova, we have included standard expectations for the incident neutrino intensities, energy distributions and interaction cross sections. The bulk of the neutrino luminosity from a core-collapse supernova is emitted during the Kelvin-Helmholtz cooling phase, which is marked by an exponentially decaying neutrino flux with a time constant of  $\sim 3$  *seconds* (31). Each flavor is described by a Fermi-Dirac distribution with a chemical potential at or near zero. At the relevant energies, the  $\mu$ - and  $\tau$ -neutrinos only interact via neutral-current processes, and therefore decouple deeper within the core (at a smaller neutrinosphere radius, the term being defined as the radius from the center at which neutrinos decouple from the dense matter), leaving them with the highest energies, estimated to be around  $\langle E_{\nu_{\mu/\tau}} \rangle \approx 25$  *MeV* or  $T \approx 8$  *MeV*. Electron-neutrinos decouple at a larger neutrinosphere radius, with the net numerical superiority of neutrons to protons resulting in the *e*-antineutrinos having higher energy than the *e*-neutrinos ( $\langle E_{\bar{\nu}_e} \rangle \approx 16$  *MeV* or  $T \approx 5$  *MeV* versus  $\langle E_{\nu_e} \rangle \approx 11$  *MeV* or  $T \approx 3.5$  *MeV* (32)).

## 2.3 *Neutrino Cross Sections Relevant to OMNIS*

OMNIS will consist of several  $\frac{1}{2}$  *kT* modules of lead and iron, which will serve as target materials. Some of the incoming neutrinos from a supernova will undergo charged-current or neutral-current interactions with the composite nuclei, resulting in neutron emission. The cross sections for such reactions depend on the neutrino energy, the Q-value for the reaction and the availability of suitable energy levels in the target nucleus. There are no available experimental data for the cross sections governing these reactions, with the exception of that for  $^{56}\text{Fe}(\nu_e, e^-)^{56}\text{Co}$  measured by the KARMEN collaboration (33), but theoretical studies have been conducted by two groups (34; 35). De-

Table 1

Comparison for single- and double-neutron events liberated from iron and lead for the different reaction channels (per  $kT$ )

Material, Event Type	CC- $\nu_e$	CC- $\bar{\nu}_e$	NC- $\nu_e$	NC- $\bar{\nu}_e$	NC- $\nu_x$	total
Pb, single-n, no osc.	59	0	8	37	677	781
Pb, double-n, no osc.	26	0	0	1	20	47
Fe, single-n, no osc.	4	5	2	6	146	163

spite qualitative agreement between the two groups, some uncertainty remains, due to the largely unknown location of the Gamow-Teller resonance relative to the neutron separation energies. These separation energies are  $10.67 \text{ MeV}$  for  $^{56}\text{Fe}$  and  $7.19 \text{ MeV}$  for  $^{208}\text{Pb}$  for single-neutron emission and  $19.78 \text{ MeV}$  and  $13.31 \text{ MeV}$ , respectively, for double-neutron emission. The single-neutron channels in lead and in iron and the two-neutron channel in lead constitute three observables closely related to the neutral-current thresholds that can be used to deduce the relevant contributions of the various neutrino flavors via the different energy dependencies of their cross sections. Both SNO and Super-Kamiokande will provide additional reaction thresholds and their data could be used in collaboration with those from OMNIS to map out the neutrino distributions.

#### 2.4 Expected Number of Events in OMNIS

All event numbers presented in this work are based on a “standard” supernova in the center of the Galaxy (distance =  $8 \text{ kpc}$ ,  $E_{tot} = 3 \times 10^{53} \text{ ergs}$ ). The number of neutrons liberated per  $kT$  in OMNIS modules of lead or iron is indicated in table 1. The cross sections for lead were taken from (34) and for iron from (35).

#### 2.5 Influence of Neutrino Oscillations on the OMNIS Yields

One possible scenario is the oscillation between  $\mu$ - or  $\tau$ -neutrinos and electron-neutrinos. The resulting higher energy for the latter, combined with the large charged-current cross section, leads to a significant increase in the overall yield in both the iron and the lead and to a dramatically increased number of double-neutron events in lead (see also table 2, which shows the result for an oscillation of all  $\mu$ -neutrinos into  $e$ -neutrinos and all  $e$ -neutrinos into  $\mu$ -neutrinos). The latter channel therefore serves as a sensitive neutrino thermometer and/or indicator for certain types of neutrino oscillations. Figure 1 shows the expected number of liberated neutrons per  $kT$  as a function of

Table 2

Comparison for single- and double-neutron events liberated from iron and lead for the different reaction channels (per  $kT$ ) with full oscillation  $\nu_\mu \leftrightarrow \nu_e$ .

Material, Event Type	CC- $\nu_e$	CC- $\bar{\nu}_e$	NC- $\nu_e$	NC- $\bar{\nu}_e$	NC- $\nu_x$	total
Pb, single-n	826	0	184	35	516	1563
Pb, double-n	1852	0	6	1	15	1874
Fe, single-n	57	5	37	6	112	217

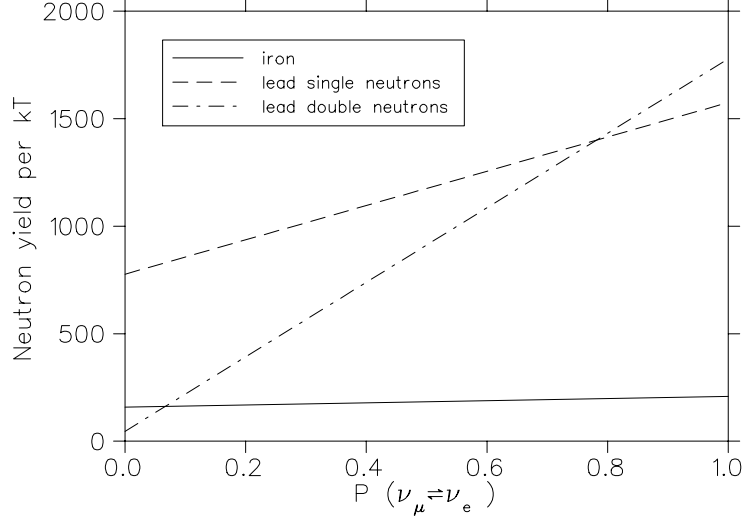


Fig. 1. Neutron Yield per  $kT$  Versus Oscillation Probability  $\nu_\mu \leftrightarrow \nu_e$ .

$P$ , the chance that a neutrino emitted from the supernova as a  $\mu$ -neutrino has oscillated into an electron-neutrino and vice versa. The ability of OMNIS to discriminate between possible oscillation scenarios is illustrated in fig. 2, where the difference between the number of single-neutron emission events and the number of two-neutron emission events observed in lead, is plotted against the number of neutron emission events in iron. This demonstrates the additional sensitivity that OMNIS has to oscillations involving sterile neutrinos.

### 3 Features of the OMNIS detector

#### 3.1 The OMNISita Test Facility

OMNIS will consist of approximately 4  $kT$  of iron and 8  $kT$  of lead modules. It will be built in the Waste Isolation Pilot Plant (WIPP) near Carlsbad, NM, which has been shown, given its background radiation and available infrastructure, to be a highly desirable site (36). At the time of this

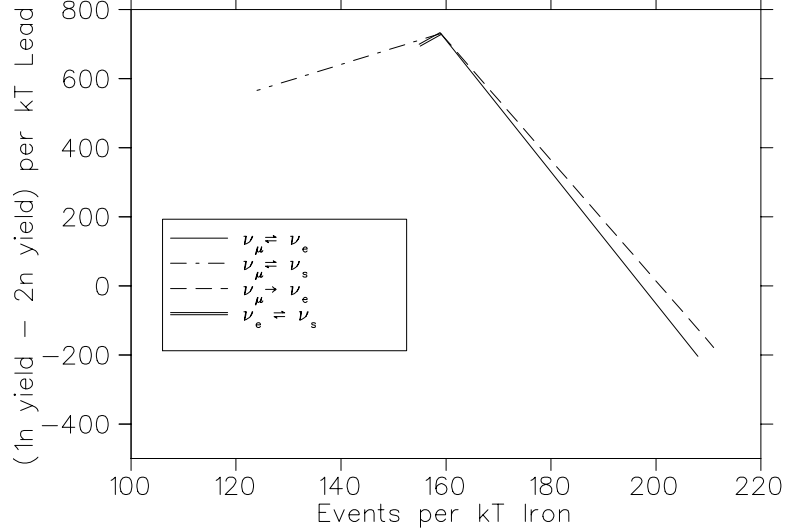


Fig. 2. Single-Neutron Yields in the Pb and Fe modules (each per  $kT$ ) for different Oscillation Schemes.

paper, a test module, OMNISita (37), is being constructed at the proposed site in order to test the predictions of the Monte Carlo code presented here, to have a test facility for the components of the OMNIS detector, and for further measurements of the radioactive and cosmic ray backgrounds.

### 3.2 *Gd loaded Liquid Scintillator for Neutron Detection*

Once neutrons are emitted, they interact with the neutron source material (Fe or Pb) and the neutron detector, assumed in the present study to be organic liquid scintillator. This serves three functions: neutron moderator, sink and detector. The use of Gd in liquid organic scintillators is well established (38), it has the highest known neutron capture cross section (39) and its solubility is high enough to make it the preferred neutron sink at this time. The possible alternatives Li and B have not been found to be soluble in organic liquids in sufficiently high concentrations and there are no known organic molecules containing Li or B that have a light yield similar to Gd loaded scintillator.

### 3.3 *Particle Propagation and Event Identification*

The neutrons produced by the neutrino interactions are expected to have initial energies of  $\sim 1 \text{ MeV}$  (35), hence moderation will primarily occur through elastic scattering off the protons in the scintillator. Our calculations show that the neutrons lose nearly all of their kinetic energy within  $\propto 100 \text{ ns}$  (see fig. 3) after emission, resulting in the production of a significant number

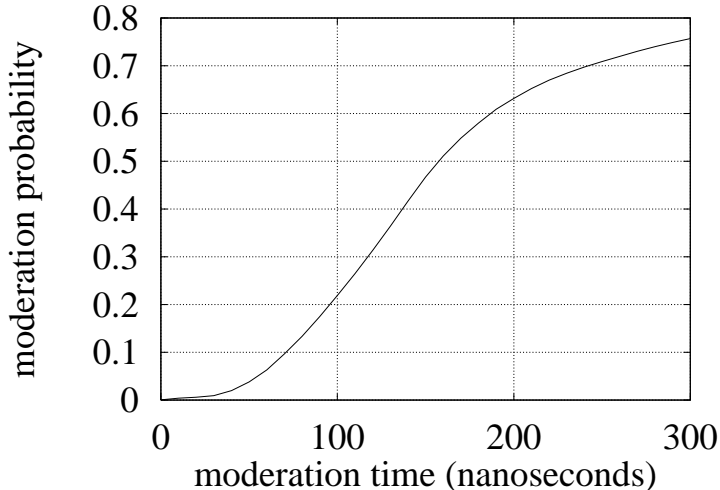


Fig. 3. Neutron Moderation Time-scale

of scintillation photons. With a 0.1% loading of Gd in the scintillator, capture occurs after  $\approx 30 \mu s$ , see also figure 4, predominantly on  $^{155/157}Gd$ . Figures 3 and 4 were generated with the optimized design for the lead modules presented below, but these time-scales are not very dependent on the detector material and geometric configuration used. Further, the capture time scales are consistent with a recent study (25; 40) performed using a prototype scintillator vessel and with similar Monte Carlo studies conducted in the past (41; 42). To enable discrimination against cosmic rays and  $\gamma$ -rays produced by the decay of radioactive impurities in the lead or iron or other detector components, a double-pulse technique with a time window between prompt and capture signals of  $\approx 50 \mu s$  will be used. The characteristic second pulse, caused by the emission of  $\gamma$ -rays following capture on Gd or H in the scintillator vessels, is used to identify the neutron pulse. The time of neutron liberation is then known within a few 100 ns. Although pulse shape discrimination might be considered as a means to identify the neutron induced events, this would be impractical for detectors as large as those required for a facility of the size of OMNIS.

### 3.4 Design Constraints

Generally, the more fine-grained neutron sources and detection elements are, the higher will be the neutron detection efficiency, since neutron energy losses and captures before they reach the detector will be minimized (38). One important cost overhead though will be the data acquisition system; this imposes a practical upper limit of several hundred independent scintillator units per  $kT$ . It is important for the lead to be free of antimony, which acts as a significant neutron sink in concentrations above  $\sim 1\%$ . Structural stability

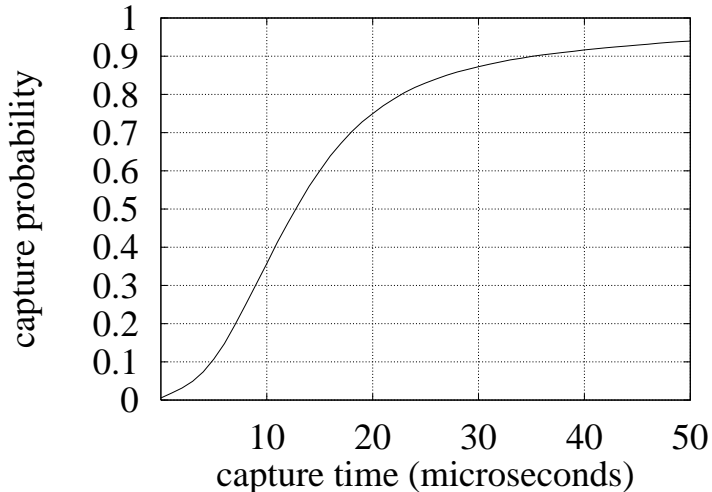


Fig. 4. Neutron Capture Time-scale

dictates lead walls with thicknesses of at least  $\sim 10$  cm, interlaced by layers of scintillator with a thickness determined by the neutron attenuation length in organic liquids, which is several cm. Rectangular acrylic tubes are assumed as scintillator containment vessels, which guide the scintillation light via total internal reflection off the acrylic/air interface. Their length will be limited by the attenuation length for photons in the scintillator, which is about 450 cm (43). The rectangular shape maximally fills out the scintillator walls, and can be manufactured for a considerably lower price than comparable units with different geometries and materials. For the regions on the tank ends not occupied by the photomultiplier tubes, a highly reflective coating of aluminum or  $Ti_2O$  is planned. A similar design was used for the Palo Verde (43) reactor experiment, which utilized acrylic vessels with 0.1% Gd loaded pseudocumene (PC) as a liquid scintillator in a solution with 60% mineral oil. The present analysis has assumed a similar material which has a high proton concentration ( $\frac{H}{C} \approx 1.64$ ), making it a good moderator. However, to increase the range over which the thickness of the detector walls can vary, stacking of the scintillator vessels in single-, double- or triple-width columns has been considered. To provide shielding from external radiation sources and reflect escaping neutrons back into the detector, each module is encased in an external lead or iron hull. Figures 5 and 6 show a schematic design for a  $\frac{1}{2}$  kT lead module.

## 4 DAMOCLES - Model for OMNIS

### 4.1 Basics of Monte Carlo Code Development

The Monte Carlo code for OMNIS was designed to provide:

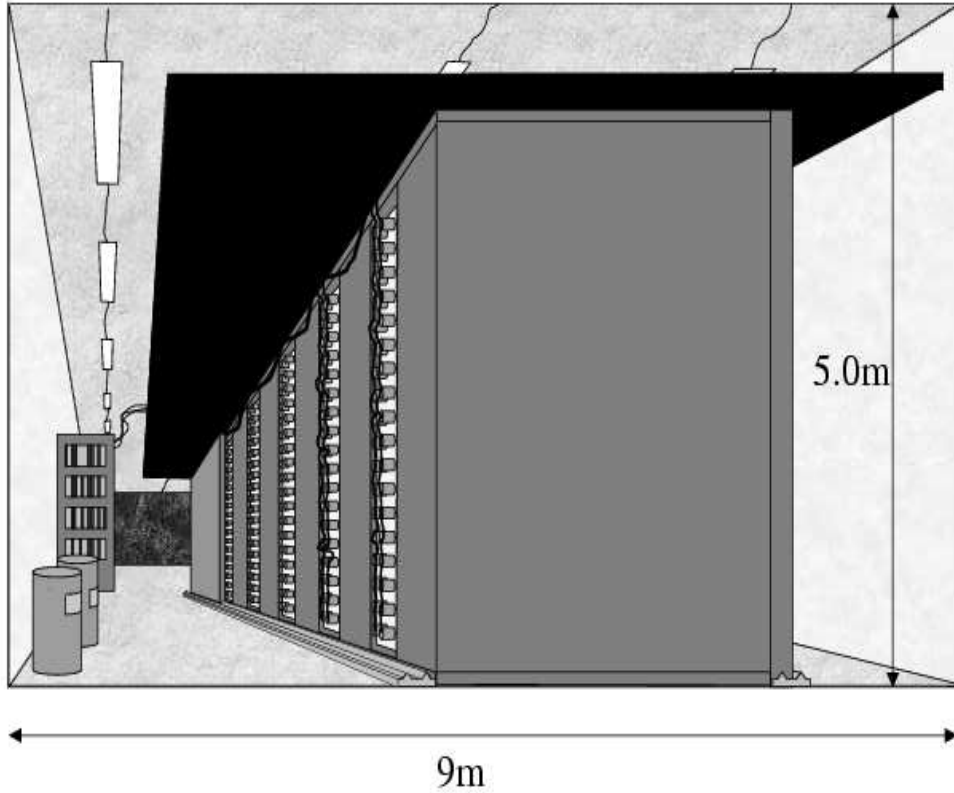


Fig. 5. Front View of an OMNIS Lead Module

- (1) Modularity: The detector consists of three principal regions, the scintillator vessels, the lead walls and the outer hull which have to be simulated in a large number of different configurations, necessitating easy control of the detector configuration. In particular, the code handles the operation of a large number of identical cells.
- (2) Parameter Control: The development of OMNIS requires the control of all parameters regarding geometry, data acquisition and the materials used, including the composition of the scintillator and possible sources of radioactive background in all detector components. That includes the cost of a given detector configuration, which is necessary to optimize cost efficiency.
- (3) Data Flow Control: In order to design the best trigger mechanism, extraction of any kind of information about particle positions and energy deposited in the detector was accommodated.
- (4) Portability: Since the simulations were performed on both single- and parallel- processor architectures, the code had to be portable among different platforms.

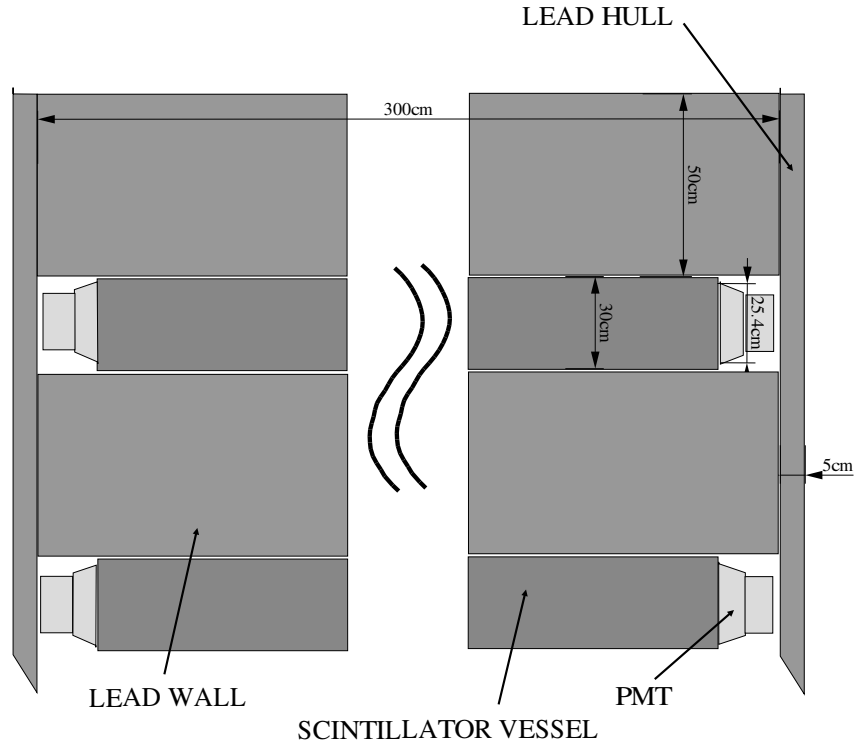


Fig. 6. Top View of Part of an OMNIS Lead Module

#### 4.2 Chronology of Events in the Monte Carlo Simulation

The treatment of events within the Monte Carlo code follows their chronology. Neutrons are first generated with appropriate energies from the spallation following neutrino interactions. Each neutron is then tracked through the detector, taking into account scattering reactions and eventual capture in one of the components or its escape from the detector. In the former case, capture  $\gamma$ -rays are traced through the detector until their eventual capture or escape. Neutrons leaving the detector are not tracked any further. The effects of including an additional external reflecting hull were tested beyond that required for shielding out external background radiation from the surrounding rock, but the resulting changes were negligible. Energy deposited into the scintillator via neutron or  $\gamma$ -interactions is converted into a number of scintillation photons, each of which is then traced until its absorption in the liquid, failure to reflect from a surface, or transmission to a photomultiplier tube.

### 4.3 Energy Spectrum of Double-Neutron Events

In the case of a double-neutron emission event, the available energy is distributed to both neutrons (35), and phase space arguments tend to equalize the energy of both neutrons. A Gaussian energy distribution was therefore assumed with the energy for each neutron limited to the total available energy, centered at and with a width of half the total energy. The influence of the width of the Gaussian on the detection efficiency for double-neutron events in lead was investigated. The narrower the Gaussian, the higher the efficiency, since the probability for one neutron having very low energy is then small. However, the double-neutron efficiency was found not to depend very sensitively on the width; the efficiency changed by only 1%, if the width is changed to either 10% or 200% of the original value.

### 4.4 Neutron Interactions

#### 4.4.1 Neutron Scattering

The total elastic scattering and absorption cross sections have been approximated using polynomials which were fitted to data from the ENDF/B file (44). Resonances were averaged over and not treated in detail, since they are limited to narrow energy ranges. At the neutron energies with which OMNIS will be dealing,  $\sim 1 \text{ MeV}$ , inelastic scattering can be neglected. The expansion of the elastic differential scattering cross section in Legendre polynomials can be written as

$$f(\cos(\theta), E) = \sum_{\ell} \left( \frac{2\ell + 1}{2} a_{\ell}(E) P_{\ell}(\cos(\theta)) \right), \quad (1)$$

where  $a_{\ell}$  are the (energy dependent) Legendre coefficients. Step functions were used based on the known Legendre coefficients as functions of the energy, and the series was terminated at  $\ell = 5$  for Fe and  $\ell = 10$  for Pb, beyond which contributions are negligible (44). Both C and H (scintillator) exhibit an s-wave distribution in the angular dependence of elastic scattering in the center of mass system for the energy ranges considered (44), thus terminating the series in eq.(1) after  $\ell = 0$ . Since its concentration is only 0.1%, and its scattering cross section is comparable to the host material, we neglect scattering from Gd.

#### 4.4.2 Neutron Capture

Neutron capture on Gd is well described by four photons with a total energy of  $7.937\text{ MeV}$  ( $^{157}\text{Gd}$ ) or  $8.536\text{ MeV}$  ( $^{155}\text{Gd}$ ) (41) with individual energies of between  $50\text{ keV}$  and  $3.5\text{ MeV}$  (45). Capture on a proton leads to the emission of a  $2.2\text{ MeV}$  photon. Capture on carbon was negligible, as was confirmed by tests. A random  $\gamma$ -ray of up to  $4\text{ MeV}$  was assumed to be produced by neutron capture on iron or lead. However, our results did not change at all if this process was left out completely, due to the high absorption cross section in Fe or Pb for  $\gamma$ -rays. For the same reason, any secondary  $\gamma$ -rays produced in inelastic scattering off Pb or Fe were found to be negligible.

#### 4.5 $\gamma$ -ray Interactions

The main energy loss channel for  $\gamma$ -rays in the energy range of interest here, up to a few  $\text{MeV}$ , in both the scintillator and the lead or iron, is Compton scattering, although all possible effects were included. The cross sections for the photoelectric effect, pair production, coherent scattering and Compton scattering were obtained from the XCOM database (46) and fitted for energy bins of  $10\text{ keV}$  ( $1\text{ keV}$  for the first  $100\text{ keV}$  in the scintillator). For the angular dependence in the differential cross section for Compton scattering the Klein-Nishina equation for photons scattering off electrons was used (47). Immediate photoelectric absorption was assumed for  $\gamma$ -rays below an energy of  $5\text{ keV}$  in Fe and Pb and  $0.5\text{ keV}$  in the scintillator. Below these respective energies, all interaction channels except photoelectric absorption are negligible, and the attenuation length is  $< 0.6\text{ mm}$  in the scintillator,  $< 0.12\text{ mm}$  in lead and  $< 0.9\text{ mm}$  in iron (46).

#### 4.6 Scintillation Photons

The liquid scintillator used in the Palo Verde experiment had a light yield of 56% of that of anthracene (43), the latter being 16 photons per  $1\text{ keV}$  (48). The neutron energy conversion efficiency due to the higher charge density caused by recoil protons is about 40% of that of the  $\gamma$ -ray conversion efficiency (49). The phototubes were assumed to detect a given photon with an efficiency of 20%. Since the tracking of the scintillation photons constitutes the bulk of computing time, only 20% of the actual number of photons were simulated, but a detection efficiency of 100% was adopted in the phototube. Scintillation photons are created with random polarization along either of two possible axes. The absorption cross section in the fluid is determined by an exponential law with an attenuation length of  $450\text{ cm}$ . If the incident angle on a surface is larger than the limit for total reflection, the photon is reflected

with 100% efficiency. The validity of this assumption was confirmed by introducing an additional finite absorption probability when a scintillation photon traverses the acrylic wall. Even for a transmission of only 95% for every reflection, the efficiency decreases by only 1%. For all other incident angles, every reflection off the walls was tested for absorption, with the reflection probability being a function of polarization and incident angle (47). If the photon hits one of the scintillator vessel ends, it is either transmitted through the photomultiplier glass face with 98% efficiency or reflected off the highly reflective rim surrounding the phototube with an efficiency of 88% for aluminum. The latter value was confirmed by measurements conducted at The Ohio State University.

#### 4.7 Event Identification

In order to discriminate against noise in the photomultiplier tubes and the electronics, a threshold was set requiring that one vessel has to register at least five photo-electrons on each end within a timebin. The length of a timebin was 100 *ns*, in accordance with the expected resolution of the data acquisition system. The threshold of five photoelectrons was chosen because it is the lowest pulse that can reliably be detected in a photomultiplier tube, but the effect of changing that value was studied as well. If two such pulses occur in the same vessel within the time-to-amplitude converter time window, i.e. if both ends of one vessel therefore fire twice, an event is registered in that vessel. Double-neutron events are identified based on two such events registering in separate vessels with the first pulse in each event happening within 100 *ns*.

#### 4.8 Intrinsic Background Radiation

Assuming that only virgin lead will be used in OMNIS, all major internal background sources in the lead modules will be elements in the natural decay series or their daughters. In lead from the DOE RUN company, a survey of samples exhibited background ranging from  $< 0.001$  to  $\sim 10 \frac{dps}{kg}$  (50), with most samples towards the lower end of the range. The dominant background source is  $^{210}Pb$  ( $T_{\frac{1}{2}} = 22.2 \text{ yr}$ ) (51). One of its daughters, the short-lived  $^{210}Bi$ , emits 1.17 *MeV*  $\gamma$ -rays (52). The absence of significant contributions from other isotopes, in particular the  $^{226}Th$  series, was recently confirmed by CEMRC in Carlsbad (53). Bremsstrahlung from the various beta-decays can be neglected, because its intensity peaks at energies below  $\sim 0.25 \text{ MeV}$ , where lead absorbs the photons very efficiently.

The total radioactivity in iron ranges between 0.00 and 0.17 decays per

second per  $kg$  above  $1 MeV$  (54). Most of the background in iron is due to  $^{60}Co$  ( $1.17 MeV$  and  $1.33 MeV$ , respectively; 60% of the background) and  $^{40}K$  ( $1.46 MeV$ ; 30% of the background). An admixture of 10%  $^{226}Th$  ( $2.6 MeV$   $\gamma$ -ray from  $^{208}Tl$ ) was assumed for higher energy  $\gamma$ -ray emissions.

Another background source is the decay of  $^{40}K$  in the glass faces of the photomultiplier tubes. The available purity ranges from 1 to 100 decays per second per  $kg$  per face (55).

The detected frequency of false  $f_F$  events should scale with the background rate  $b$  as

$$f_F = k_1 b f_R + k_2 b^2, \quad (2)$$

where  $k_1$  and  $k_2$  are constants depending on the trigger time window and  $f_R$  is the frequency of real neutron events. The linear term in  $b$  enhances the detection efficiency by providing a missing second pulse to go with either the prompt (neutron-) or delayed ( $\gamma$ -) pulse. The quadratic term in  $b$  describes coincident double-pulse triggers from the background, in which both pulses within the trigger window are caused by background radiation. It is important for the latter term to be small at all times, even when there is no supernova, in order to avoid false alarms. During the actual supernova pulse, the background contribution is then dominated by the linear term.

The number of background  $\gamma$ -rays occurring in a time bin, as implemented in the code, is Poisson distributed:

$$p_k = \frac{\lambda^k}{k!} e^{-\lambda}, \quad (3)$$

where  $k$  denotes the resulting number of background events and  $\lambda$  is the number of events per time bin.

## 5 Efficiency Optimization

### 5.1 Optimization of Detector Dimensions

The basic philosophy adopted was to optimize the cost efficiency of the OMNIS modules rather than the absolute efficiency. Cost efficiency here is defined as efficiency divided by cost times  $US\$ 10^7$ , which ranges between 0 and 2. The dependence of the detection efficiency and cost efficiency on

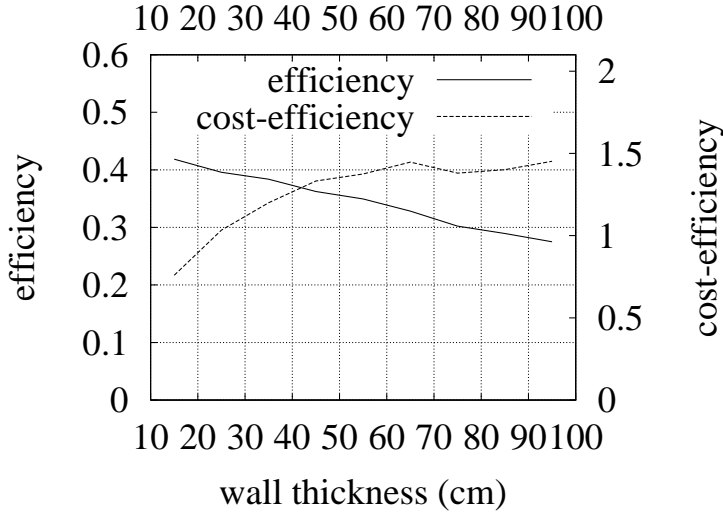


Fig. 7. Efficiency and cost efficiency vs. lead wall thickness for single-neutron events.

the parameters scintillator vessel dimensions, lead/iron wall thickness, hull thickness, photon threshold and neutron energy was investigated.

### 5.1.1 The Lead Modules

The most cost efficient way to detect single-neutron events was found to be a design with single scintillator columns with photomultiplier tubes (PMTs) of 10 *in* (25.4 *cm*) diameter. Double and triple columns of photomultiplier tubes with smaller PMTs were also considered. However, scintillator vessels with a diameter that is considerably larger than the attenuation length of both neutrons and  $\gamma$ -rays dramatically increase the detection efficiency and decrease the number of scintillator vessels needed for a given mass of lead. This leads to a 50% better cost efficiency for single columns with 25.4 *cm*-PMTs compared to double columns of 12.7 *cm*-PMTs. For double-neutron events, the greater stopping power for larger vessels also leads to a higher cost efficiency, more than compensating for the detrimental effect of a less fine-grained detector on the detection of two neutrons in two separate detectors.

The cost efficiency for both single- and double-neutron event detection rises as the lead wall thickness increases, then flattens out for a thickness of 50 *cm* (fig.7 and 8), although from a pure efficiency-point of view, somewhat thinner lead walls would be preferable.

As expected from the bulk photon attenuation length in the scintillator, a vessel length of 300 *cm* maximizes both efficiency and cost efficiency for single- and especially double-neutron event detection (fig. 9, 10).

The cost efficiency for single-neutron events might be optimized for ves-

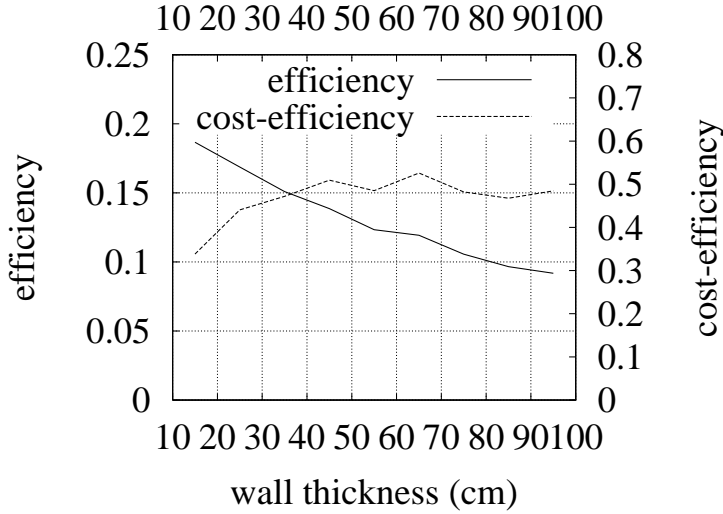


Fig. 8. Efficiency and cost efficiency vs. lead wall thickness for double-neutron events.

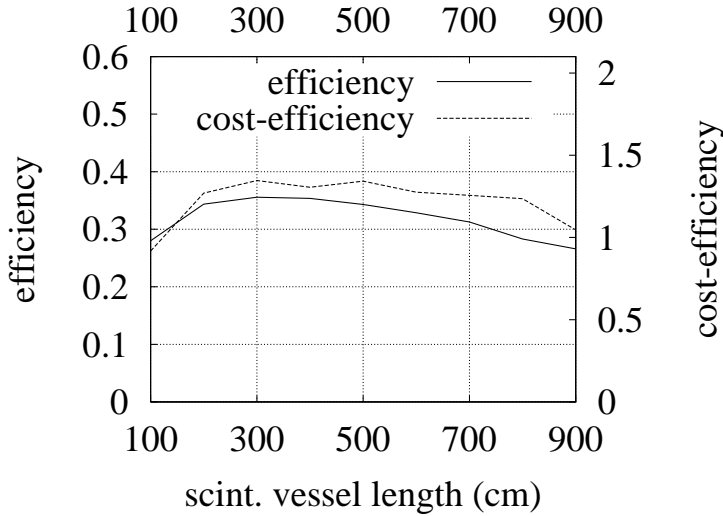


Fig. 9. Efficiency and cost efficiency vs. scintillator vessel length in the OMNIS lead module for single-neutron events.

sels with widths slightly larger than required by the size of the PMTs, the fewer number of PMTs necessary might more than compensate for the lower efficiency for each single scintillator vessel. There is a slight decrease in the cost efficiency with increasing vessel width (by 5 – 10%) and a slight increase (by  $\sim 3\%$ ) with vessel height, when increased from 30 *cm* to 45 *cm*. However, the cost efficiency for two-neutron events requires that the vessel dimensions should only exceed the PMT dimensions by a few *cm* at most, since a decrease of the cost efficiency for two-neutron events by  $\sim 20\%$  is observed when both vessel width and height are increased from 30 *cm* to 45 *cm*.

The calculation does not consider the cost for the electronics, although it will be small compared to the cost for the scintillator vessels and the PMTs.

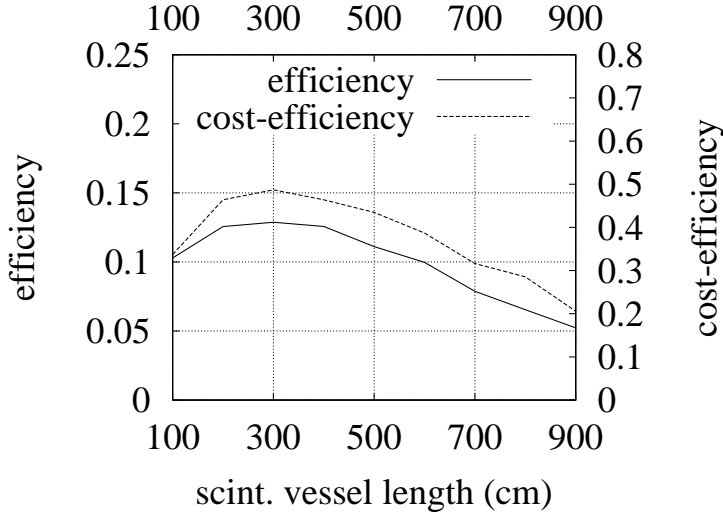


Fig. 10. Efficiency and cost efficiency vs. scintillator vessel length in the OMNIS lead module for double-neutron events.

However, it decreases with an increasing number of scintillator vessels. We have considered using four PMTs with diameters of  $12.7\text{ cm}$  instead of one  $25.4\text{ cm}$ -PMT per scintillator vessel. This would provide the same fractional coverage of the vessel face area, but on top of the approximately four-fold cost for the electronics, one larger PMT is less than four times as expensive as four smaller PMTs.

A thicker lead hull slightly decreases both the detection efficiency and the cost efficiency of the detector, since more of the neutrons that are produced are lost. We therefore plan to make the hull only as thick as necessary to attenuate the external background sources in the WIPP cave.

The detection efficiency for single-neutron events is constant for neutron energies beyond a few hundred  $keV$  (fig.11). For double-neutron events, the available energy gets distributed to two neutrons. Hence, the detection efficiency for those events starts showing an asymptotic behavior only for energies above  $\sim 1\text{ MeV}$  (fig.12).

The detection efficiency is still satisfactory, if the pulse threshold has to be set higher than the five photoelectrons assumed (fig.13). However, as expected, the double-neutron efficiency decreases more rapidly for higher thresholds (fig.14).

### 5.1.2 The Iron Modules

The iron modules have to be optimized only with respect to the cost efficiency for single-neutron events. The optimum dimensions of the scintillator containment vessels and the wall thicknesses are similar to those for the lead

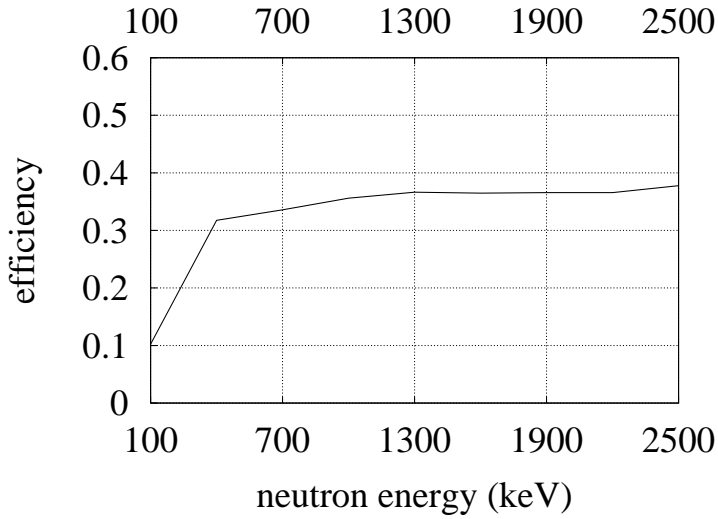


Fig. 11. Efficiency vs. neutron energy in the OMNIS lead module for single-neutron events.

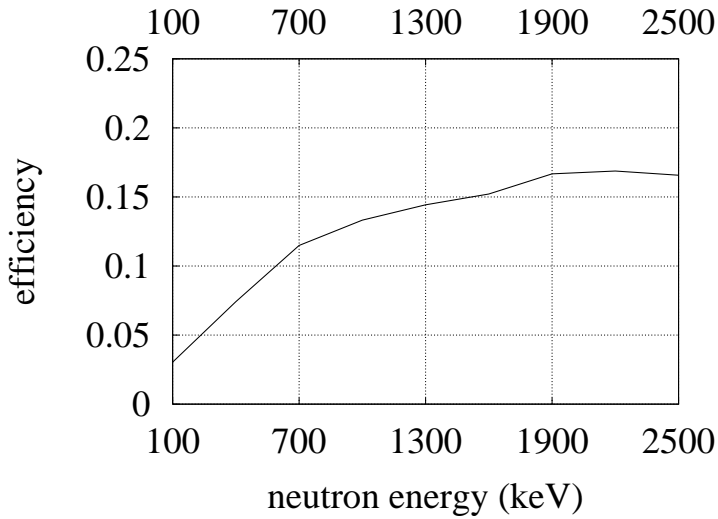


Fig. 12. Efficiency vs. neutron energy in the OMNIS lead module for double-neutron events.

modules. As in the case of lead, an iron detector with fewer and larger scintillator vessels is both more efficient and cost efficient. The dependence of the cost efficiency on the vessel width and height suggests more elongated vessels along the vertical direction than in the case of lead. The detection efficiency becomes flat for higher neutron energies than in the case of lead (fig.15), which is due to the fact that more energy is lost in an average elastic collision with an iron nucleus.

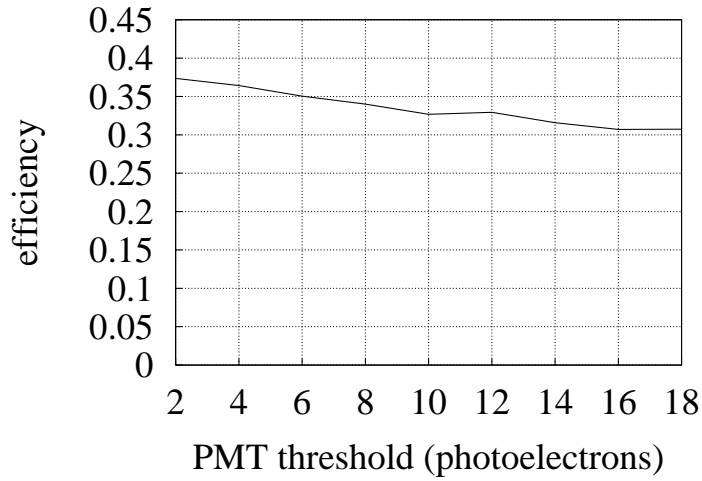


Fig. 13. Efficiency vs. photoelectron threshold in the OMNIS lead module for single-neutron events.

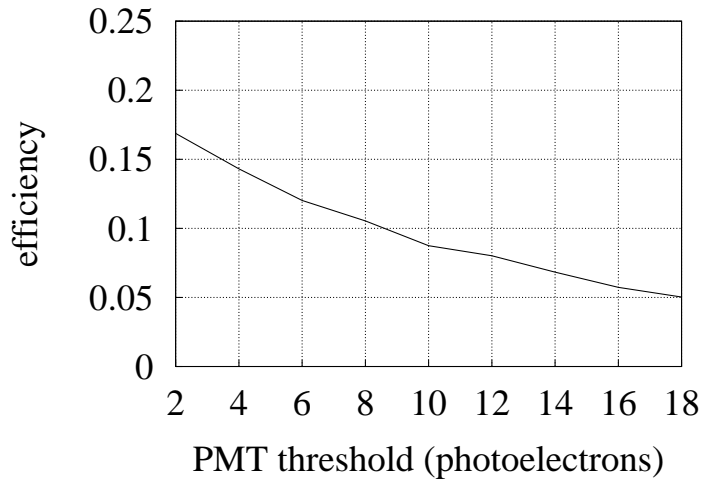


Fig. 14. Efficiency vs. photoelectron threshold in the OMNIS lead module for double-neutron events.

### 5.1.3 Summary for Optimized Dimensions

Table 3 summarizes the optimized dimensions for  $\frac{1}{2}kT$  lead and iron modules, stacked in single scintillator vessel columns (with photomultiplier tubes with diameters of 25.4 cm on each end).

## 5.2 Influence of the Background

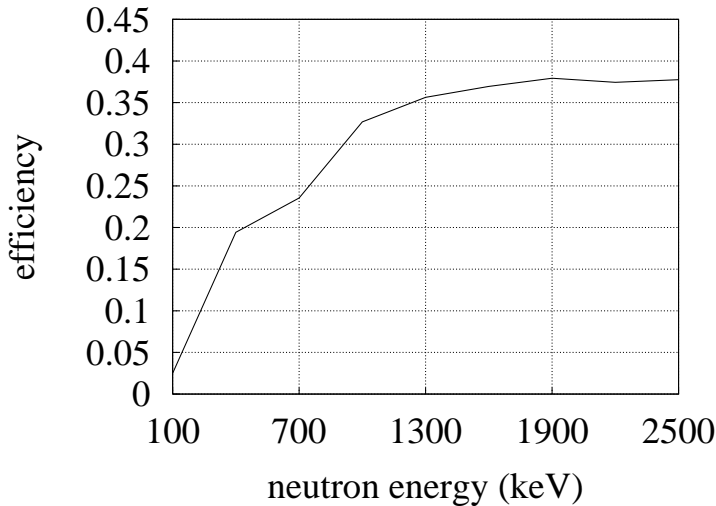


Fig. 15. Efficiency vs. neutron energy in the OMNIS iron module.

Table 3

Summary of optimized detector dimensions for the OMNIS lead and iron modules.

Material	wall(cm)	hull(cm)	vessel(L(cm)xW(cm)xH(cm))
Pb	50	15	300 x 30 x 30
Fe	50	25	300 x 30 x 45

### 5.2.1 The Lead Modules

The detected false event rate in OMNIS in the absence of emitted neutrons is shown in fig. 16. This confirms radiological analyses (51) which show that if the bulk impurity rate in lead can be maintained below  $0.1 \frac{Bq}{kg}$ , then the false event rate in OMNIS will be less than  $\sim 1$  per second. The ability to detect neutrino events at late times after the core bounce is determined by the influence of the radioactive background on a sparse neutron signal, with a typical time interval between two neutrons being long compared to the dead time of the detector, taken to be  $80 \mu s$ . The apparent efficiency of a sparse neutron signal relative to the efficiency without background is shown in fig. 17, which shows that a tolerance of  $0.1 \frac{Bq}{kg}$  is also acceptable in this respect.

Figures 18 and 19 show the false event rate due to  $^{40}K$  decays in the photomultiplier glass faces without neutrons and the relative apparent efficiency in the presence of a sparse neutron signal. A tolerance limit of  $100 Bq$  has been adopted for each PMT.

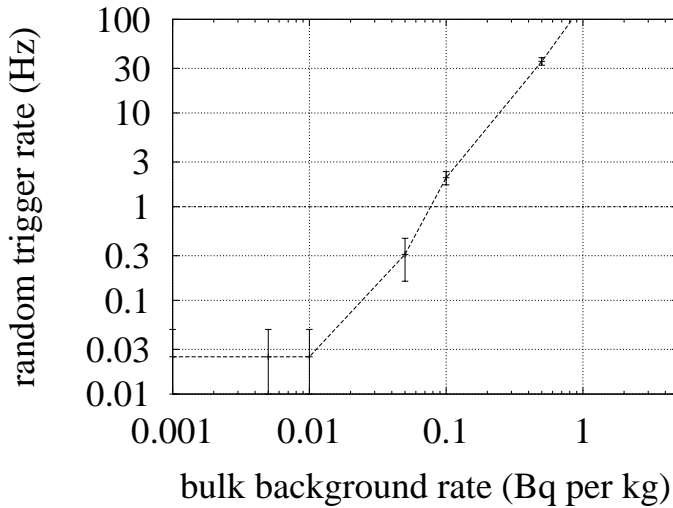


Fig. 16. False Event Rate per  $kT$  due to Bulk Background in OMNIS Pb Modules.

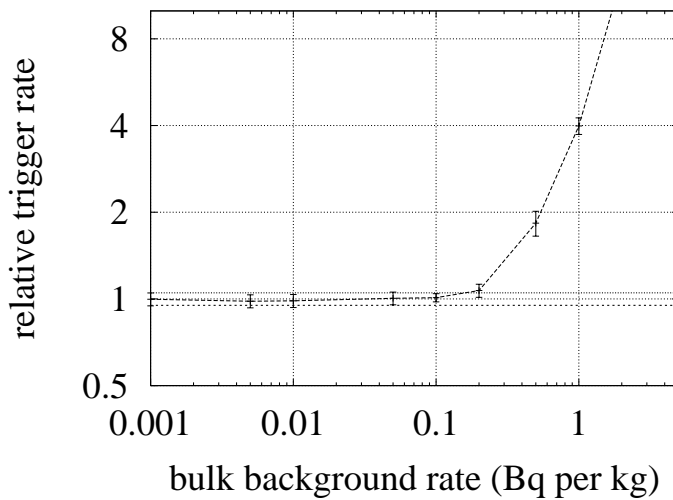


Fig. 17. Apparent Enhancement of Sparse Neutron Signal due to Bulk Background in OMNIS Pb Modules. The two horizontal lines indicate a  $\pm 5\%$  change relative to zero background.

### 5.2.2 The Iron Modules

Due to the higher energy of the background  $\gamma$ -rays and their longer attenuation length in iron, the requirements for its purity have to be more stringent than for lead. The resulting tolerance limit for the bulk background in the iron used is  $\sim 0.05 \frac{Bq}{kg}$  (see figures 20 and 21). This also appears to be consistent with radiological analyses (54). The allowed background rate in the photomultiplier glass faces is, however, the same as in lead, 100  $Bq$  per PMT (see figures 22 and 23).

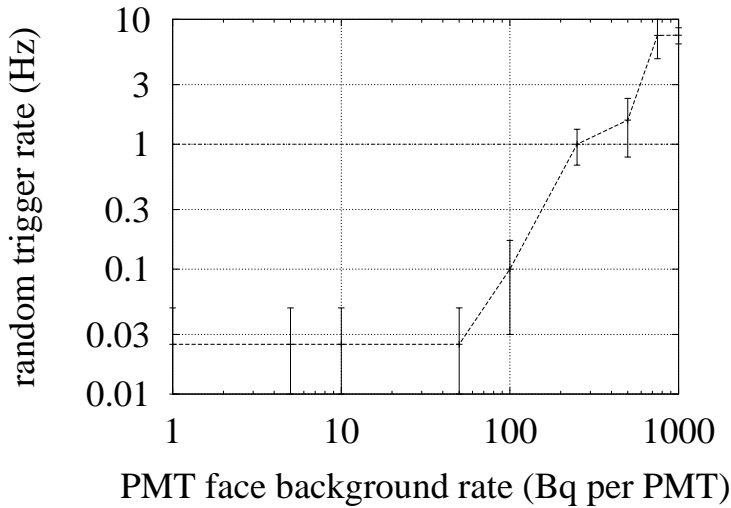


Fig. 18. False Event Rate per  $kT$  due to  $^{40}K$  decays in PMT faces in OMNIS Pb Modules.

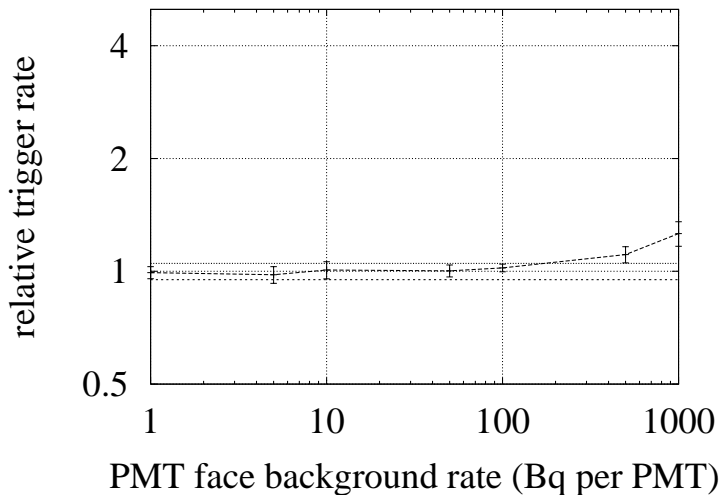


Fig. 19. Apparent Enhancement of Sparse Neutron Signal due to  $^{40}K$  decays in PMT in OMNIS Pb Modules. The two horizontal lines indicate a  $\pm 5\%$  change relative to zero background.

### 5.3 Dependence on Supernova Distance

If one event strobe is used for an entire detector module, there is a minimum distance of the supernova for which its dead time becomes critical for reliable event detection. Assuming one detected neutron event to trigger a strobe with  $80 \mu s$  for a lead module of  $\frac{1}{2} kT$  (with 60 scintillator vessels), dead time losses become significant for supernovae closer than  $2 kpc$ , which represents only a few percent of the Galaxy. Table 4, generated with a simulated supernova neutrino burst (56), shows the number of detected events

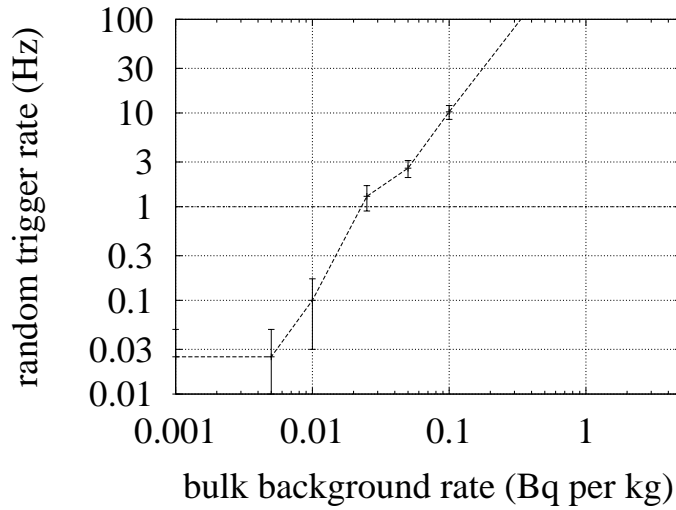


Fig. 20. False Event Rate per  $kT$  due to Bulk Background in OMNIS Fe Modules.

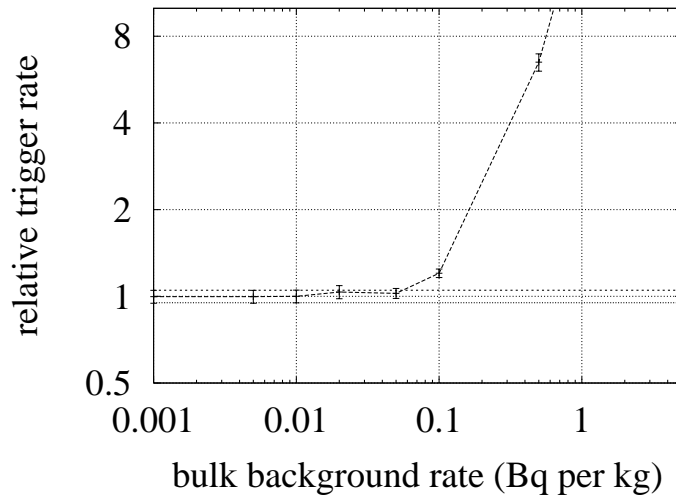


Fig. 21. Apparent Enhancement of Sparse Neutron Signal due to Bulk Background in OMNIS Fe Modules. The two horizontal lines indicate a  $\pm 5\%$  change relative to zero background.

versus supernova distance. The case without dead time is shown for reference. We intend to utilize a sufficiently sophisticated data acquisition system such that it can handle the higher neutron liberation rates associated with close supernovae in at least one module, thus precluding the excessive loss of high resolution data obtainable from a close supernova.

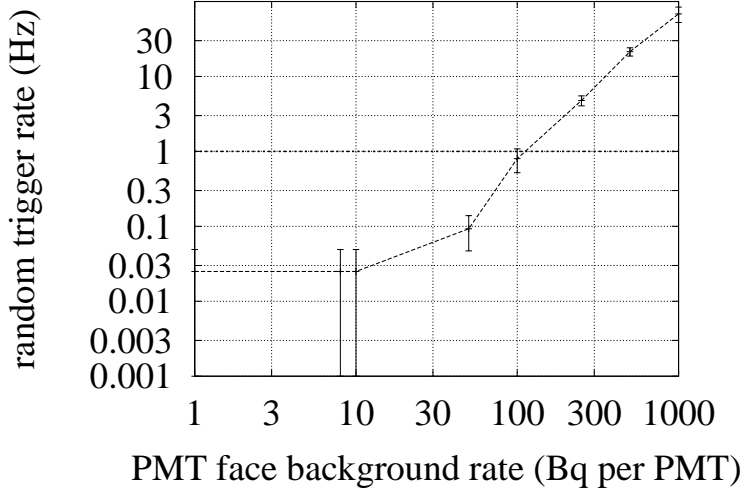


Fig. 22. False Event Rate per  $kT$  due to  $^{40}K$  decays in PMT faces in OMNIS Fe Modules.

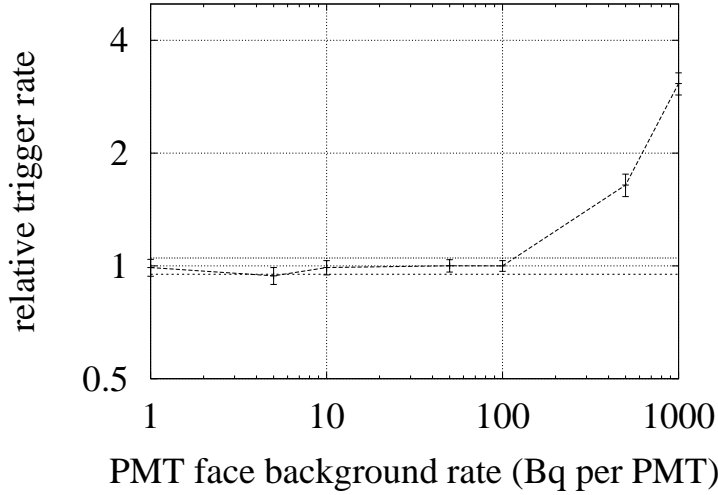


Fig. 23. Apparent Enhancement of Sparse Neutron Signal due to  $^{40}K$  decays in PMT faces in OMNIS Fe Modules. The two horizontal lines indicate a  $\pm 5\%$  change relative to zero background.

Table 4

Number of detected neutron events versus supernova distance for 16  $\frac{1}{2}kT$  Pb modules.

Dead Time ( $\mu s$ )	0.20 kpc	0.50 kpc	1.0 kpc	2.0 kpc	4.0 kpc	8.0 kpc	16 kpc
80	$0.888 \times 10^6$	$0.293 \times 10^6$	95400	26200	6740	1730	440
0	$2.86 \times 10^6$	$0.458 \times 10^6$	112000	27500	6860	1740	440

## 6 Summary

Once built, OMNIS will fill in the long perceived need for a large neutral-current supernova neutrino detector. The neutrino fluxes for the different flavors will be measured using the yields from multiple threshold processes, single- and double-neutron emission in lead and single-neutron emission in iron. The time resolution is only limited by the event rate (and therefore the distance) of the supernova. This will reveal unprecedented insight into the core-collapse supernova mechanism and might, for the first time ever, open up a window onto the black hole formation mechanism, and possibly enable the observation of the different neutrinosphere radii for different neutrino flavors. In addition, OMNIS is capable of placing new limits on the allowed neutrino mass - mixing angle phase space using time-of-flight methods for different flavors and the relative yields for the different neutron liberation channels.

The generic designs for the OMNIS modules are walls of lead or iron, interlaced with stacks of vessels containing organic liquid scintillator loaded with Gd. A double-pulse trigger with the capture  $\gamma$ -ray pulse giving the confirmation to the preceding neutron pulse in the same scintillator vessel was identified as an effective means to discriminate neutron events against the radioactive background. Using the Monte Carlo code DAMOCLES, developed for OMNIS, optimum configurations for the detector geometry of the iron and the lead modules were found with respect to the maximum number of events for a given unit cost. The resulting detection efficiencies for  $\frac{1}{2}$   $kT$  modules are  $\sim 38\%$  for single- and  $\sim 13\%$  for double-neutrons in lead and  $\sim 34\%$  for iron. However, the detection efficiency might improve due to lower possible thresholds when off-line analysis of the data is performed. Given the predicted numbers of neutrons liberated, we estimate a total of 8  $kT$  of lead and 4  $kT$  of iron is needed for the OMNIS detector.

The false trigger rate caused by the radioactive background in the presence or absence of a supernova neutrino pulse was investigated with the result that tolerance levels lie within the range found in commercially available materials. The criterion was a false rate of  $\sim \frac{1}{sec.}$ , low enough to still detect a sparse neutron signal.

The overall neutron trigger rate is below 10  $kHz$  for a  $\frac{1}{2}$   $kT$  module and a “standard” Galactic supernova (56; 57), which would enable the use of a common trigger gate for the entire detector. If, however, a supernova occurs at distances less than  $\sim 1$   $kpc$ , the typical time between two-neutron events at the peak of the signal becomes lower than typical dead times of  $\sim 80$   $\mu s$ , in which case common trigger gates for smaller numbers of or even individual photomultiplier tubes become desirable in order to measure the peak neutron liberation rate, at least for part of OMNIS.

## 7 Acknowledgements

This work is supported by the National Science Foundation, grant number PHY-9901241 and by The Ohio State University. We would especially like to thank the Carlsbad Area Office of the Department of Energy and the Waste Isolation Division of the Westinghouse Corporation which operate the Waste Isolation Pilot Plant for their support. The Monte Carlo simulations were supported in part by a grant from the Ohio Supercomputing Center.

## References

- [1] K. Hirata *et al.* (Kamiokande II collaboration), Phys. Rev. Lett. **58** (1987) 1490.
- [2] R.M. Bionta *et al.* (IMB collaboration), Phys. Rev. Lett. **58** (1987) 1494.
- [3] A. Burrows, Nucl. Phys. A **606** (1996) 151.
- [4] W. Keil, H.T. Janka and G. Raffelt, Phys. Rev. D **51** (1995) 6635.
- [5] A. Mezzacappa *et al.*, LANL preprint server astro-ph/0005366 v3 27 Oct 2000
- [6] E. Baron and J. Cooperstein, Astrophys. J. **353** (1990) 597, and references therein.
- [7] H.A. Bethe Astrophys. J. **412** (1993) 192.
- [8] M. Boezio *et al.*, Phys. Rev. Lett. **82** 24 (1999) 4757.
- [9] R. Becker-Szendy *et al.*, Phys. Rev. D **46** 9 (1992) 3720.
- [10] W.W.M. Allison *et al.*, Phys. Lett. B, **449** (1999) 137.
- [11] Y. Fukuda *et al.* (Kamiokande collaboration) Phys. Rev. Lett. **77** 9 (1996) 1683.
- [12] N. Fornengo, M.C. Gonzalez-Garcia and J.W.F. Valle, Nucl. Phys. B **580** (2000) 58.
- [13] B.T. Cleveland *et al.*, Nucl. Phys. B, Proc. Suppl. **38** (1995) 47.
- [14] K.S. Hirata *et al.*, Phys. Lett. B **280** (1992) 146.
- [15] S. Wanninger *et al.*, Phys. Rev. Lett. **83** 6 (1999) 1088.
- [16] J.N. Abdurashitov *et al.*, Phys. Rev. Lett. **83** 23 (1999) 4686.
- [17] Y. Fukuda *et al.* (Super-Kamiokande collaboration), Phys. Rev. Lett. **82** (1999) 2430.
- [18] M.C. Gonzalez-Garcia, P.C. de Holanda, C. Pena-Garay and J.W.F. Valle, Nucl. Phys. B **573** (2000) 3.
- [19] S.M. Bilenky, C. Giunti and C.W. Kim, Int. J. Mod. Phys. A **15** (2000) 625.
- [20] S.E. Woosley, J.R. Wilson, G.J. Mathews, R.D. Hoffman and B.S. Meyer, AstroPhys. J. **433** (1994) 229.
- [21] K. Takahashi, J. Wittl and H.T. Janka, Astron. AstroPhys. **286** (1994)

- 857-869; J. Wittig, H.T. Janka and K. Takahashi, *Astron. AstroPhys.* **286** (1994) 841.
- [22] D.O. Caldwell, G.M. Fuller and Y.Z. Qian, *Phys. Rev. D* **61** (2000) 123005.
- [23] G.C. McLaughlin, J.M. Fetter, A.B. Balantekin and G.M. Fuller, *Phys. Rev. C* **59** 5 (1999) 2873.
- [24] D.B. Cline, G.M. Fuller, W.P. Hong, B. Meyer and J. Wilson, *Phys. Rev. D* **50** (1994) 720.
- [25] R.N. Boyd and A.St. J. Murphy, *Next Generation Nucleon Decay and Neutrino Detector*, AIP Conf. Proc., **533** 132.
- [26] K. Langanke, P. Vogel and E. Kolbe, *Phys. Rev. Lett.* **76** (1996) 2629.
- [27] M. Vagins, University of California at Irvine, private communication.
- [28] J.F. Beacom and P. Vogel, *Phys. Rev. D* **58** (1998) 093012; *Phys. Rev. D* **58** (1998) 053010.
- [29] T.W. Baumgarte, H.T. Janka, W. Keil, S.L. Shapiro and S.A Teukolsky, *AstroPhys. J.* **468** (1996) 823.
- [30] J.F. Beacom, R.N. Boyd and A. Mezzacappa, *Phys. Rev. Lett.* **85** (2000) 3568; LANL preprint server, astro-ph/0010398 19 Oct 2000.
- [31] J.A. Pons, S. Reddy, M. Prakash, J.M. Lattimer and J.A. Miralles, *AstroPhys. J.* **513** (1999) 780.
- [32] Y.Z. Qian, G.M. Fuller, G.J. Mathews, R.W. Mayle, J.R. Wilson and S.E. Woosley, *Phys. Rev. Lett.* **71** 13 (1993) 1965.
- [33] R. Maschuw, *Prog. Part. Nucl. Phys.* **40** (1998) 183.
- [34] G.M. Fuller, W.C. Haxton and G.C. McLaughlin, *Phys. Rev. D* **59** (1999) 085005.
- [35] E. Kolbe and K. Langanke, LANL preprint server, nucl-th/0003060, 27 Mar 2000.
- [36] M.J. Balbes, R.N. Boyd, J.D. Kalen, C.A. Mitchell, M. Hencheck, E.R. Sugarbaker, J.D. Vandegriff, D.A. Sanders and S.D. Lieberwirth, *Nucl. Instr. Meth. A* **399** (1997) 269.
- [37] A.St. J. Murphy, internal document: <http://www.physics.ohio-state.edu/~asmurphy/omnis/omnisita/index.html>, Oct. 2000.
- [38] P.F. Smith, *Astropart. Phys.* **8** (1997) 27.
- [39] H. Rauch, M. Zawisky, Ch. Stellmach and P. Geltenbort, *Phys. Rev. Lett.* **83** 24 (1999) 4955.
- [40] A.St. J. Murphy, internal document: <http://www.physics.ohio-state.edu/~asmurphy/proto-11-98.html>, Nov. 1998.
- [41] A. Trzcinski and B. Zwieglinski, *Acta Phys. Polon. B* **28** (1997) 145.
- [42] A. Trzcinski, B. Zwieglinski, U. Lynen and J. Pochodzalla, *J. Neutron Research* **8** (1999) 85.
- [43] A.G. Piepke, S.W. Moser and V.M. Novikov, *Nucl. Instr. Meth. A* **432** (1999)392.
- [44] Evaluated Nuclear Data File/B 6 of the National Nuclear Data Center, <http://t2.lanl.gov/cgi-bin/nuclides/endind>.
- [45] National Nuclear Data Center, Brookhaven Na-

- tional Laboratory, Thermal Neutron Capture Database, <http://www.nndc.bnl.gov/wallet/tnc/capgam.shtml>.
- [46] <http://physics.nist.gov/PhysRefData/Xcom/Text/XCOM.html>.
- [47] J.D. Jackson *Classical Electrodynamics*, 2nd Edition, p.682. Wiley, New York, London, Sydney, Toronto, 1975.
- [48] R.C. Sangster and J.W. Irwine, *J. Chem. Phys.* **24** (1956) 670.
- [49] W.J. Price, *Nuclear Radiation Detection*, 2nd Edition, McGraw-Hill, New York, 1964
- [50] J. O'Reilly, Lead Smelting Division, The Doe Run Company, 881 Main Str., Herculaneum, MO, 63048, private communication.
- [51] R. Brodzinski, Pacific Northwest National Laboratory, private communication.
- [52] R.E. Lapp, H.L. Andrews, *Nuclear Radiation Physics*, 2nd Edition, Prentice Hall, New York, 1955.
- [53] Joel Webb, Carlsbad Environmental Monitoring and Research Center, private communication.
- [54] Maury C. Goodman, High Energy Physics Division, Argonne National Laboratory, private communication.
- [55] Lee Nowell, LANCO International Inc. (Distribution of Photonis Imaging Sensors), 200 Market Place, Suite 140, Roswell, GA 30075, USA.
- [56] A. Burrows, *Ann. Rev. Nucl. Part. Sci.* **40** (1990) 181.
- [57] A. Mezzacappa, Oak Ridge National Laboratory, private communication.